2012

Sulfosalt melts and heavy metal (As-Sb-Bi-Sn-Pb-Tl) fractionation during volcanic gas expansion: The El Indio (Chile) paleo-fumarole

Richard Henley
Australian National University

John Mavrogenes
Australian National University

Dominique Tanner
Australian National University, dtanner@uow.edu.au

Publication Details

Henley, R. W., Mavrogenes, J. & Tanner, D. (2012). Sulfosalt melts and heavy metal (As-Sb-Bi-Sn-Pb-Tl) fractionation during volcanic gas expansion: The El Indio (Chile) paleo-fumarole. Geofluids, 12 (3), 199-215.

Sulfosalt melts and heavy metal (As-Sb-Bi-Sn-Pb-Tl) fractionation during volcanic gas expansion: The El Indio (Chile) paleo-fumarole

Abstract

High-sulfidation vein gold deposits such as El Indio, Chile, formed in fracture arrays <1000m beneath paleo-solfatara in volcanic terranes. Stable isotope data have confirmed a predominance of magmatic vapor during the deposition of arsenic-rich sulfide-sulfosalt assemblages in this deposit. These provide a unique opportunity to analyze the processes and products of high-temperature volcanic gas expansion in fractures that form the otherwise inaccessible infrastructure deep inside equivalent present-day fumaroles. We provide field emission scanning electron microscope and LA-ICP-MS micro-analytical data for the wide range of>heavy, semi-metals and metalloids (arsenic, antimony, bismuth, tin, silver, gold, tellurium and selenium) in the complex pyrite-enargite-Fe-tennantite assemblages from Copper Stage mineralization in the El Indio deposit. These data document the progressive fractionation of antimony and other heavy metals, such as bismuth, during crystallization from a sulfosalt melt that condensed from expanding vapor at about 15MPa (150bars) and >650°C following higher temperature vapor deposition of crystalline pyrite and enargite. The sulfosalt melt aggressively corroded the earlier enargite and pyrite and hosts clusters of distinctive euhedral quartz crystals. The crystallizing sulfosalt melt also trapped an abundance of vugs within which heavy metal sulfide and sulfosalt crystals grew together with K-Al silicates and fluorapatite. These data and their geologic context suggest that, in high-temperature fumaroles on modern active volcanoes, over 90% of the arsenic content of the primary magmatic vapor (perhaps 2000mgkg -1) was precipitated subsurface as sulfosalt. Subsurface fractionation may also account for the range of exotic Pb-Sn-Bi-Se sulfosalts observed in fumarole sublimates on active volcanoes such as Vulcano, Italy, as well as on extra-terrestrial volcanoes such as Maxwell Montes, Venus.

Publication Details

Henley, R. W., Mavrogenes, J. & Tanner, D. (2012). Sulfosalt melts and heavy metal (As-Sb-Bi-Sn-Pb-Tl) fractionation during volcanic gas expansion: The El Indio (Chile) paleo-fumarole. Geofluids, 12 (3), 199-215.

GEOFLUIDS
Geofluids (2012) 12, 199–215 doi: 10.1111/j.1468-8123.2011.00357.x

Sulfosalt melts and heavy metal (As-Sb-Bi-Sn-Pb-Tl) fractionation during volcanic gas expansion: the El Indio (Chile) paleo-fumarole

R. W. HENLEY, J. MAVROGENES AND D. TANNER
Research School of Earth Sciences, Australian National University, Canberra, ACT, Australia

ABSTRACT

High-sulfidation vein gold deposits such as El Indio, Chile, formed in fracture arrays <1000 m beneath paleo-solfatara in volcanic terranes. Stable isotope data have confirmed a predominance of magmatic vapor during the deposition of arsenic-rich sulfide–sulfosalt assemblages in this deposit. These provide a unique opportunity to analyze the processes and products of high-temperature volcanic gas expansion in fractures that form the otherwise inaccessible infrastructure deep inside equivalent present-day fumaroles. We provide field emission scanning electron microscope and LA-ICP-MS micro-analytical data for the wide range of heavy, semi-metals and metalloids (arsenic, antimony, bismuth, tin, silver, gold, tellurium and selenium) in the complex pyrite-enargite-Fe-tennantite assemblages from Copper Stage mineralization in the El Indio deposit. These data document the progressive fractionation of antimony and other heavy metals, such as bismuth, during crystallization from a sulfosalt melt that condensed from expanding vapor at about 15 MPa (150 bars) and >650°C following higher temperature vapor deposition of crystalline pyrite and enargite. The sulfosalt melt aggressively corroded the earlier enargite and pyrite and hosts clusters of distinctive euhedral quartz crystals. The crystallizing sulfosalt melt also trapped an abundance of vugs within which heavy metal sulfide and sulfosalt crystals grew together with K-Al silicates and fluorapatite. These data and their geologic context suggest that, in high-temperature fumaroles on modern active volcanoes, over 90% of the arsenic content of the primary magmatic vapor (perhaps 2000 mg kg^{-1}) was precipitated subsurface as sulfosalt. Subsurface fractionation may also account for the range of exotic Pb-Sn-Bi-Se sulfosalts observed in fumarole sublimates on active volcanoes such as Vulcano, Italy, as well as on extra-terrestrial volcanoes such as Maxwell Montes, Venus.

Key words: antimony, arsenic, bismuth, El Indio, enargite, fumarole, gold, high sulfidation, magmatic vapor, solfatara

Received 10 August 2011; accepted 8 November 2011

Corresponding author: Richard W. Henley, Research School of Earth Sciences, Australian National University, Canberra, ACT, Australia.
Email: r.143.henley@gmail.com.

Geofluids (2012) **12**, 199–215

INTRODUCTION

One of the beauties of magmatic-hydrothermal ore deposits lies in the insights that they provide to otherwise inaccessible crustal processes in and around volcanoes. For example, heavy metals[1] (As, Sb, Bi, etc.) discharge continually from active volcanic-gas fumaroles with temperatures up to about 1100°C, yet what controls the abundance of these environmentally toxic elements in these discharges is poorly understood. Direct sampling is hazardous, fraught with practical difficulty and limited to surface discharges that may already have deposited key component elements subsurface during expansion of the gas phase to atmospheric pressure. One way of gaining insight into these environments is through analysis of their fossil equivalents.

Stable isotope data from 'high sulfidation' enargite-gold deposits around the world consistently show that the fluid responsible for their formation was dominantly magmatic in origin with very limited admixture of groundwater (Deyell *et al.* 2004, 2005; Rye 2005). These and fluid inclusion data commonly infer the formation of 'silica-alunite' wallrock

[1]A heavy metal is a member of a loosely-defined subset of elements that exhibit metallic properties. It mainly includes the transition metals, some metalloids, lanthanides, and actinides as well as the Group Va (15) elements, As, Sb, and Bi.

alteration from acidic condensate derived from low salinity magmatic vapor and temperatures up to at least 500°C (Henley & Berger 2011). In the Maricunga Belt, straddling the Argentine-Chile border, a number of such deposits have been described in detail. The 8.0–8.9 Ma Pascua-Lama and Tambo deposits, for example, are associated with blankets of advanced argillic alteration (Chouinard *et al.* 2005; Deyell *et al.* 2004) that are interpreted as equivalent to the extensive solfatara observed in modern day volcanic belts. By contrast, a number of high-sulfidation enargite-gold deposits, such as Summitville, Colorado (Bethke *et al.* 2005) and El Indio (Jannas *et al.* 1999), occur as veins in association with advanced argillic wallrock alteration and are interpreted from their geology as having formed within 1500 m of the paleosurface as feeders to higher level but now eroded solfatara (Berger & Henley 2011; Henley & Berger 2011). As such, these vein deposits are the fossil equivalents of the feeders for modern day active fumaroles[2] so that the mineral assemblages preserved within them enable us to at least partially unravel some of the reaction sequences that occur as volcanic gas expands within high-temperature fumaroles in modern day volcanoes.

In this study, we provide new data for mineral compositions and sulfide–sulfosalt phase relations at El Indio. They enable a new understanding of the processes controlling the relative abundance of heavy and semi-metals and metalloids in volcanic fumarolic discharges and their sublimates on Earth as well as on volcanically active planets; bismuth-lead sulfides and sulfosalts, for example, have been deduced from radar reflectance data to constitute the high level 'metallic snow' capping on volcanoes on Venus (Schaefer & Fegley 2004).

SULFIDE–SULFOSALT MINERAL ASSEMBLAGES IN THE EL INDIO VEINS

The 7 Ma high-sulfidation gold-silver-enargite (Cu_3AsS_4) deposit at El Indio, Chile, formed as a sequence of veins at about 650–1150 m below the surface of a dacitic volcanic complex (Jannas *et al.* 1999; Fig. 24). Vein mineralization occurs within a 2 km^2 section of a more extensive (30–40 km^2) region that is characterized by advanced argillic to argillic alteration (Jannas 1995) within a sequence of andesitic to dacitic volcaniclastic rocks. The sulfide–sulfosalt ore assemblages discussed here developed sequentially (Jannas *et al.* 1999) within a syn-volcanic array of active faults and related fractures. Importantly, they postdate intense wallrock alteration and silicification – a timing relationship interpretable as the consequence of structurally driven coupled changes in fracture permeability and heat transfer from the expanding magmatic gas (Berger & Henley 2011). Figure 1 provides a first glimpse of the typical and often vuggy, sulfide–sulfosalt–quartz relationships that we document here for the early ore stage ('Copper Stage' – as detailed below) at El Indio. These assemblages immediately pose a number of questions. For example, how was the open space created within the pre-existing pyrite in which the distinctive tennantite-quartz assemblages developed? How were the components of the sulfosalts and their inclusions (Cu, Fe, As, Sb, S, Te, Ag, Bi, Tl, Sn) transported into this space along with silica? How may we account for the occurrence of discrete sulfides (e.g., galena and other heavy metal sulfides), sulfosalt minerals and tiny gold crystal clusters in some vugs while others are empty?

Figure 2 shows the locations of the sulfosalt-sulfide samples in the context of the geology of the El Indio deposit[3] and the relative time sequence of mineral formation[4] within the vein system (Fig. 2C). Jannas *et al.* (1990, 1999) recognized two principal stages of sulfide–sulfosalt mineralization in veins that postdate earlier silica-alunite-pyrophyllite wallrock alteration. The first – the Copper Stage – was initiated by pyrite deposition followed by a succession of subparallel bands and cross-cutting veinlets dominated by enargite, tennantite, and chalcopyrite. The second – the Gold Stage – was dominated by silica, sometimes chalcedonic, veins that contain a range of more complex sulfosalt and telluride minerals, and in contrast to the earlier, sulfide–sulfosalt stages appear to preserve isotopic evidence for groundwater mixing with magmatic vapor[5] at this late stage (Jannas *et al.* 1990, 1999).

[2]The term fumarole is applied generically to any vapor discharge whether from an active volcano or from much lower temperature steam-heated alteration blankets above geothermal systems. The isotope signatures of the latter are dominated by evaporative and mixing processes involving groundwater (Henley & Stewart 1983), in contrast to those of high-temperature fumaroles that are dominated by volcanic gas with very limited entrainment of groundwater (Botcharnikov *et al.* 2003). Since the stable isotope compositions interpreted from high sulfidation deposits are dominantly of magmatic affinity, we here restrict our usage of the term to fumarole to high-temperature (> approximately 600°C) vents that discharge gas mixtures dominated by volcanic gas.

[3]The sample suite was kindly provided by Francois Robert and the staff of Barrick (Chile) to represent a wide range of sulfosalt assemblages across the mine. Table 1 provides sample locations using mine grid coordinates.

[4]The term paragenesis is commonly used to infer deposit-scale mineral sequencing in a vein deposit. We note that in complex vein arrays, there is no certainty that a given sequence of minerals at different locations represents synchronicity. Here we prefer to recognize a sequence of reactions and their products that provide information about the response of the transport fluid to physicochemical changes as they occur in different parts of the vein array.

[5]Here the generic term magmatic vapor refers to the gas phase released from sub-volcanic magmatic systems. As noted elsewhere (Henley & Berger 2011), it is important to note that magmatic gases expand to the surface via fracture arrays through the crust and hence from a magmatic gas reservoir rather than necessarily from a specific body of magma as is commonly assumed.

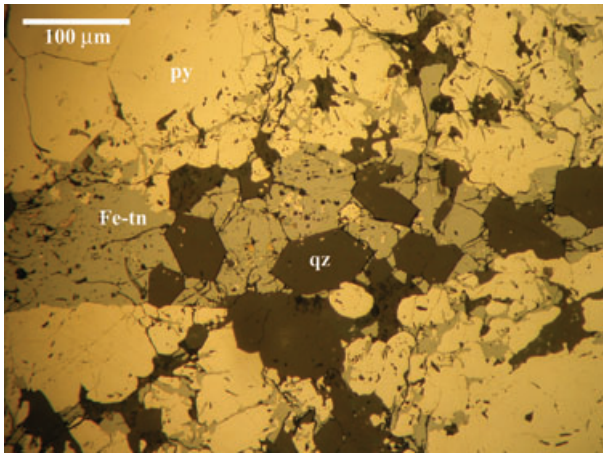

Fig. 1. Reflected light image of typical relationships between Fe-tennantite (Fe-tn), pyrite (py) and euhedral quartz (qz) in the Copper Stage of mineralisation at the El Indio enargite-tennantite gold deposit. Note the relative timing of Fe-tennantite, pyrite, quartz and the occlusion of sulfosalt inclusions in the euhedral quartz. Sample EI1300.

This study focuses on the Copper Stage vein assemblages and specifically the common compositional and textural themes that underlie the extreme compositional and textural heterogeneity seen across the entire sample suite. Mineral compositions and stoichiometry were obtained using a Zeiss Ultraplus field emission scanning electron microscope (FESEM) equipped with an INCA Energy 450 System and an Oxford Light Element EDS Detector. To minimize the required atomic number, absorption and fluorescence corrections, appropriate well-characterized minerals were used for calibration purposes. Operating conditions were 15 kV and 1 or 0.6 nA depending upon which of two detectors was available. Cu-Fe-S phase compositions were cross-checked using a JEOL 6400 SEM equipped with an Oxford Link light element EDS detector and Oxford ISIS Quant software.

The published oxygen and hydrogen isotope data used for interpreting the provenance of vein fluids (Jannas *et al.* 1999) were limited to minerals including alunite and sericite in the wallrock assemblages and suggested a fluid mixture containing at least 60% magmatic fluid. This contrasts with the much larger magmatic proportion evident at the higher level, solfatara-related, Tambo and Pascua-Lama gold-silver deposits (Deyell *et al.* 2004). New SHRIMP oxygen isotope data for discrete quartz crystals extracted from the early copper-rich ore assemblages (D. Tanner, R. Henley, J. Mavrogenes, P. Holden, T. Mernagh, unpublished data) have confirmed a much higher proportion of magmatic fluid in the ore stage at El Indio consistent with these adjacent deposits.

Pyrite and tennantite are the most abundant minerals in the sample suite along with enargite and abundant quartz as distinctive euhedral crystals (Fig. 1). Nonstoichiometry is ubiquitous in sulfosalt minerals, but for comparative purposes the ideal formula recommended by Moelo *et al.* (2008, p.27) for the isotypic tennantite-tetrahedrite series is useful; '$A_6(B, C)_6X_4Y_{12}Z$, where A is Cu or Ag in triangular coordination, B is Cu or Ag in tetrahedral coordination, C is generally a divalent metal (typically Fe or Zn, but also Hg, Mn, Cd, …) in the same tetrahedral coordination, X is Sb, As, Bi or Te in trigonal pyramidal coordination, Y is S or Se in tetrahedral coordination, and Z is S or Se in a special octahedral coordination'. In the El Indio suite, Sb ↔ As and Fe ↔ Cu substitution are most prominent with Bi, Te and Se and other heavy metals only locally above detection (0.1–0.2 wt %) as detailed below. As Fe-substitution is ubiquitous from about 0.7 to 1.7 atoms per formula unit (29–30 atoms), we use the term *Fe-tennantite* in reference to this phase. Se is a trace component and does not significantly substitute for S, so we have referenced Fe-tennantite compositions to S = 13 using the generic formula for the tennantite-tetrahedrite solid solution series $(Cu, Ag)_{10}(Fe, Cu)_2(Sb, As, Bi, Te)_4S_{13}$. Referenced to this composition, Cu+Fe in the Fe-tennantite ranges from 11.7 to 12.5 atoms per formula unit. A small analytical error for Cu may occur as discussed by Makovicky & Karup-Møller (1994), but is not relevant to the substitutions in the X site that are of principal interest here. For convenience we here define an Antimony Number, N_{Sb}, to refer to the atomic ratio Sb/(As + Sb) expressed as percent and equivalent to the relative proportion of Fe-substituted tetrahedrite in the solid solution. N_{Sb} varies from 0% to 77% within this sample suite.

Figure 1 shows how the 'Copper Stage' tennantite-quartz assemblages infill fractures and open space in earlier unzoned pyrite; the As content of the pyrite is below detection (approximately 0.1 wt %) consistent with the electron microprobe data of Jannas (1995). These relationships are detailed at the micron scale in Fig. 3 and show that pyrite has been corroded to give complex but smooth boundaries against the subsequent Fe-tennantite. The latter was introduced together with silica via a network of fractures (Fig. 3G). Its composition is variable with N_{Sb} in this example, ranging from 1% to 32.3% (mean = 12.6%) and from 2.4 to 6.3 (mean = 4.5) in atomic % Fe. Figure 3B–F shows that the Fe-tennantite infill is itself comprised of distinctive compositional domains. Domain boundaries are curved and in some cases highlighted by apparently exsolved 'blebs' of $CuFeS_2$. Figure 3E shows crystallization of Te-Pb-Bi-enriched Fe-tennantite occurring adjacent to low N_{Sb}, high Fe, Fe-tennantite. Tellurium is generally below detection (<0.1–0.2 wt%), reaching 3 atomic percent at N_s > approximately 22 (Fig. 3D). The Fe-tennantite here is metal deficient (10.7–11.3) relative to the idealized formula (A+B+C =12) and consistent with the range of electron microprobe analyses of Jannas (1995).

In Fig. 4A,B, the Fe-tennantite domains are distinct. The major domains are rimmed by an abundance of small vugs

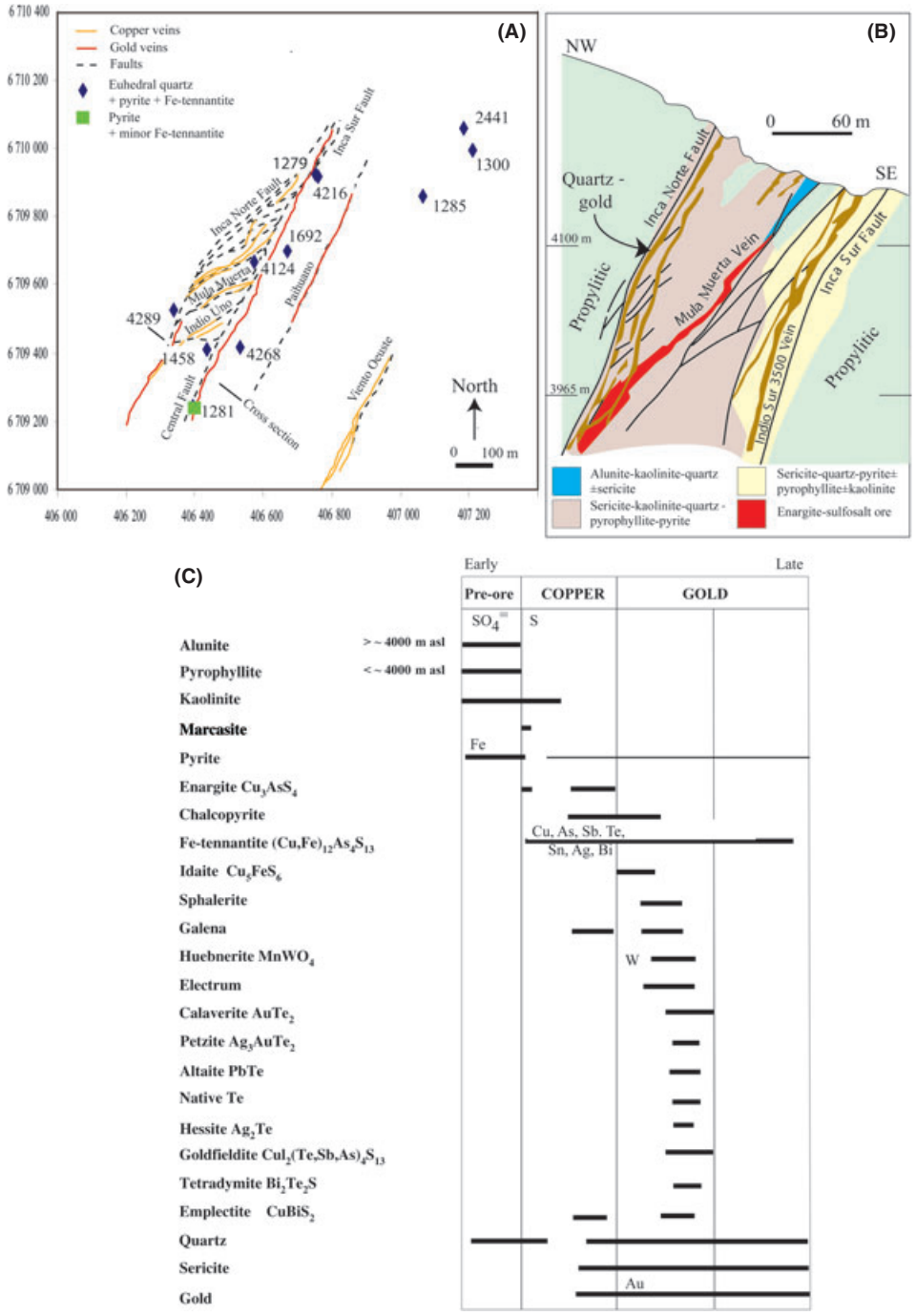

Fig. 2. (A) Projection of relative sample locations onto the generalized geological map of the El Indio Mine 3965-Level (3965 m above sea level). (B) illustrative cross section showing relationship of fault arrays, mineralized fractures and alteration and (C) sequence of mineral reaction products during mineralisation; modified to include data reported in this paper (e.g. the presence of trace tin, bismuth and tellurium in the Fe-tennantite). A–C are modified from Jannas (1995) and Jannas *et al.* (1999).

reminiscent of the vuggy margins of pillow basalts, have curved boundaries and an inter-domain region comprised of zoned Fe-tennantite crystallites and blebs of chalcopyrite. Larger ragged-margin vugs characterize the core of the rimmed domains where N_{Sb} ranges from 3.3% to 4% and Fe from 4.4 to 5.0 atomic %. Large vugs and clusters of euhedral quartz crystals are primarily, but not exclusively associated with the interior of the rimmed domains. The zoned sulfosalt between these domains is comprised of Fe-tennantite with similar iron content, but in contrast,

Table 1 Sample locations for the El Indio sample suite: map coordinates and elevation (*Z* meters above sea level). For relative locations in the context of the geology see Fig. 2.

Sample number	*X* m	*Y* m	*Z* masl
1279	406753.67	6709922.68	3817.14
1281	406392.82	6709244.91	3690.85
1285	407065.56	6709858.6	4116.92
1300	407211.45	6709991.64	3811.37
1458	406433.96	6709409.06	3726.87
1692	406668.62	6709701.05	3698.98
2441	407185.53	6710057.74	3925.26
4124	406574.59	6709669.69	3982.69
4216	406760.78	6709916.61	3788.68
4268	406532.89	6709416.77	4063.7
4289	406339.17	6709523.65	3890.88

compositional boundaries are curved and clearly defined. There are oscillations in N_{Sb} that are clearly shown by the brightness contrast in back-scattered images with N_{Sb} varying systematically from about 4 to at least 77% with tellurium and bismuth both below detection (< approximately 0.1wt %).

Enargite, Cu_3AsS_4, is far less common than Fe-tennantite in the sample suite. Figure 5A shows early enargite, characterized by well-developed cleavage, aggressively replaced by Fe-tennantite but retaining its cryptic crystal outline, identifiable in both reflected light and FESEM backscatter and secondary electron images (Fig. 5A,B). Here, vugs are common along the enargite cleavage but appear less common in Fe-tennantite. The bright area in the right edge of Fig. 5B is one of the rare, localized occurrence (see detail below) of bismuth enrichment to 1.2 atomic % Bi[6] within Fe-tennantite (N_{Sb} = 4–13%) that also hosts isolated tiny vugs enclosing galena.

Laser ablation inductively coupled mass spectrometry (LA-ICP-MS) was used to traverse this area (Fig. 5B). A slit was placed into the laser aperture and traversed the sample at 1 μm sec^{-1}. Scans were performed at a repetition rate of 7 Hz, keeping the gas signal constant between 45 and 50 mJ. The gas background was collected before and after ablation. As the results could not be normalized, raw data are presented (Fig. 5C). The distinction of enargite from Fe-tennantite is evident from the relative iron concentration. It is evident from the co-variation of trace element concentrations that the replacement of enargite by Fe-tennantite was accompanied by introduction of Sb, Ag, Bi, Hg, Te and Sn. These highly variable relative concentrations are consistent with their occurrence, along with Pb as PbS, as discrete inclusions in the sulfosalts. These relationships show that the reaction of enargite to Fe-tennantite was not simply a response to a change in temperature or the relative activity of sulfur that redistributed trace elements from the original enargite, but that these heavier elements were introduced during the replacement reaction. The complexity of the replacement is illustrated in Fig. 5D,E.

Figure 6A provides an example of the relationship between $CuFe_{1-x}S$ ([Cu+Fe]/S = 49.7–50.3%) and Fe-tennantite, (N_{Sb} = 1.7–39.6) with up to 0.7 atomic % Bi (see also Mavrogenes *et al.* 2010; Fig. 2B,C) associated with vugs in a Fe-tennantite matrix. The largest of these vugs contains crystalline K-mica (K/Al, 0.32, Al/Si, 0.7). Figure 6B–F shows examples of the aggressive reaction relationship between Fe-tennantite and pyrite that is common throughout the sample suite. A distinct monomineralic rim of chalcopyrite is sometimes preserved around pyrite remnants (Fig. 6D) but generally, corroded pyrite interfaces directly with Fe-tennantite while $CuFe_{1-x}S_2$ may form independent crack-fill (Fig. 6C) textures through pyrite. In some samples, a cryptic boundary of the original pyrite is preserved by the distribution of $CuFe_{1-x}S_2$ blebs (see Mavrogenes *et al.* 2010; Fig. 2A). Jannas (1995) notes that $CuFe_{1-x}S_2$ forms separate veins in some parts of the deposit.

While pyrite and enargite corrosion and replacement by Fe-tennantite are common, bismuthinite (Bi_2S_3)-$(CuBi)_{1-y}S_2$-Fe-tennantite (N_{Sb} = 14.1–35.3) assemblages occur locally replacing earlier Fe-tennantite and infilling cracks through pyrite (Figs 5B and 7). Here the tennantite does not contain detectable tellurium, but bismuth ranges from 0.2 to 2.4 atomic %, equivalent to about 0.1 atoms per formula unit. Even more interesting is the spectacular zonation of bismuth (Fig. 7C) extending outward from a distinctive radiating fracture array in pyrite across pre-existing Fe-tennantite. Figure 7D shows bismuthinite $([Cu,Bi]_{1-y}S_2)$-Fe-tennantite intergrowths, and Figure 7E shows how the bismuth-rich assemblage corrodes earlier Fe-tennantite (N_{Sb} = 0–2.2, with Te and Bi below detection) and pyrite.

Micron-scale and larger vugs are common throughout the Fe-tennantite-enargite assemblages (Fig. 8, and see Mavrogenes *et al.* 2010). Many appear to be empty but others have well-developed linings with discrete crystals (Fig. 8B–D). It is important to note that quite different mineral phases occur in vugs that may only be a few tens of microns apart. For example, clusters of gold crystals (Fig. 8C) and Cu_2S vug linings (Fig. 8D) occur with distinctive PbS inclusions in Fe-tennantite that replaced earlier enargite alongside a quartz crystal (Fig. 8E). Figure 6G shows pyrite with a vug that contains Fe-tennantite-chalcopyrite intergrowths together with empty space or vapor. Isolated tin-minerals such as kuramite ($\sim Cu_3SnS_4$) and thallium-rich inclusions occasionally occur in the Fe-tennantite (Fig. 6F).

[6]There are inevitable peak overlap issues when separating heavy metal spectra for analysis. Here we only report bismuth, tellurium, and lead enrichment at concentrations well above the detection limit and where there is good peak discrimination.

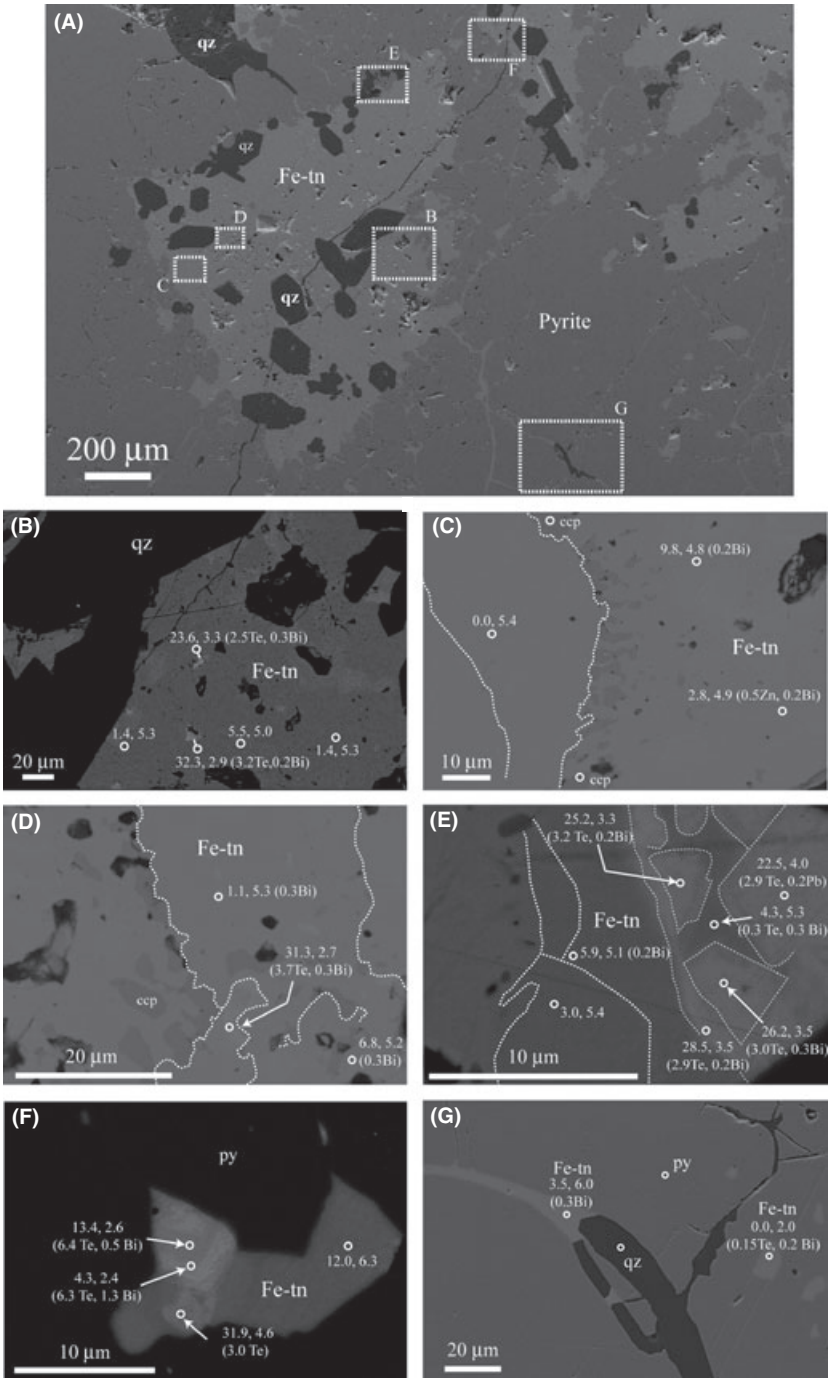

Fig. 3. Back scattered images of sulfosalt assemblages, analytical spot data shown in white as N_{Sb}, Fe atom percent where $N_{Sb} = 100 \times Sb/(As + Sb)$ with Sb and As in atomic percent. Multiple analyses of Fe-tennantite assemblages within open space in fractured pyrite illustrating the range of tennantite compositions along with variable substitution of Bi and Te. Note the distribution of euhedral quartz crystals, curved domain boundaries and crystallization of discrete phases within domains. Sample EI1300T. The textural relationship shown in (F) may be interpreted as a wetting relationship (A. Tomkins, pers. comm. 2011).

One of the most striking relationships throughout the sample suite is the occurrence of quartz as euhedral, often doubly terminated, crystals (Fig. 1 and Mavrogenes *et al.* 2010; Fig. 1) within Fe-tennantite – but not within pyrite. Figure 8G provides an example of the development of a single euhedral quartz crystal within a matrix of Fe-tennantite ($N_{Sb} = 13.1$), Fe and Bi = 3.9 and 1.4 atomic %, respectively. In Figure 5E, a quartz cluster inside enargite has occluded Fe-tennantite and is rimmed by Fe-tennantite, suggesting that a volume change attended quartz growth simultaneous with crystallization of Fe-tennantite. Tanner *et al.* (submitted) have identified residual silica hydrates within the quartz crystals indicating that the crystallization of quartz occurred by dehydration from a higher temperature silica hydrate. Homogenization of 'primary' vapor-rich inclusions can therefore only provide an estimate (455°C, Mavrogenes *et al.* 2010) of the final crystallization temperature of quartz from the primary silica

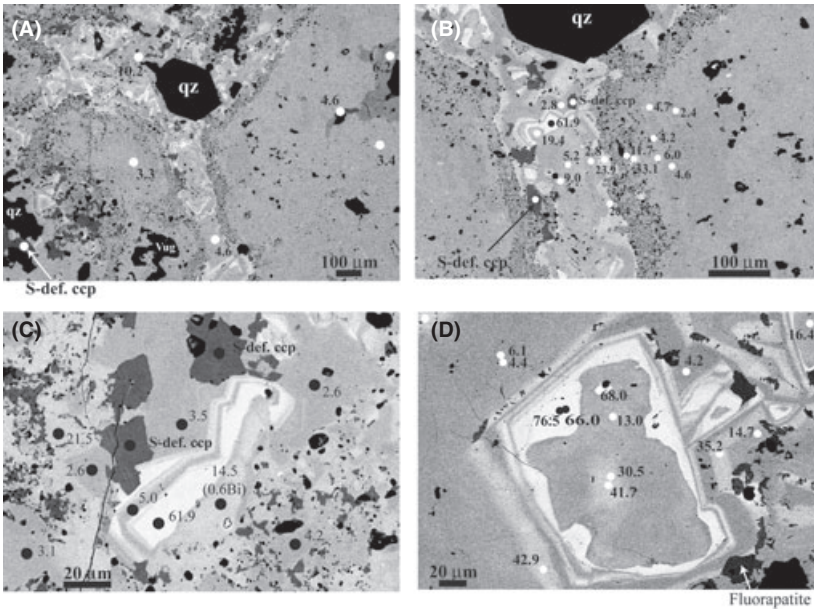

Fig. 4. Back scattered images of sulfosalt assemblages. (A,B) Relationship of low N_{Sb} Fe-tennantite with distinct vuggy margins to highly fractionated Fe-tennantite (to N_{Sb} = 75.6), and euhedral quartz. (C,D) Complex oscillatory N_{Sb} zonation of Fe-tennantite as discrete domains within vuggy low N_{Sb} Fe-tennantite. Note the occurrence of fluorapatite and corroded sulfur-deficient chalcopyrite in (D). Sample EI4216FIB. ccp, chalcopyrite.

hydrate rather than the deposition temperature of the primary assemblage from which they formed. Relationships between N_{Sb} zoning and euhedral quartz crystals (e.g., Figs 5E and 8G, and Mavrogenes *et al.* 2010; Fig. 1C) support this interpretation. The presence of sulfide- and sulfosalt-melt inclusions in quartz (Fig. 9) confirms co-precipitation of the precursor silica hydrate and sulfosalt melt.

DISCUSSION

Nuccio *et al.* (1999) have shown that high-temperature fumaroles (i.e., > approximately 600°C) in active volcanic environments form by isenthalpic expansion of magmatic vapor through available high permeability fracture arrays. Henley & Berger (2011) argued from a review of the geological setting and geochemistry of high-sulfidation lode gold deposits worldwide, including El Indio, that all were formed in a similar shallow subfumarolic setting with abundant evidence of high-temperature gradients to >500°C preserved in the presulfide silica-alunite wallrock alteration that effectively sealed and insulated the sulfide-stage vapor expansion from surrounding groundwater flow (Henley & Berger 2011, Fig. 7).

The mineral relationships shown in Figs 1–8 and their associated analyses illustrate a complex rapidly evolving sulfide–sulfosalt–silica depositional setting, 650–1150 m below the paleo-surface at El Indio. Our data show that in the Copper Stage (Fig. 2C), pyrite was deposited first in available fracture space and, following *its* fracturing, was succeeded by localized deposition of crystalline enargite in open space. Enargite was followed by Fe-tennantite that filled available space and aggressively corroded the earlier crystalline enargite and pyrite. The preservation of cryptic crystal faces of replaced enargite and pyrite and the widespread occurrence of vugs provide evidence, as discussed below, of high-temperature diffusion-controlled replacement reactions in the presence of a vapor phase. The Fe-tennantite developed a range of heterogeneous textures with discrete domains fractionating progressively to higher N_{Sb} with localized enrichment in bismuth and other heavy metals.

The combination of these textural and compositional relationships, the contemporaneous evolution of distinctive euhedral quartz crystals with extreme oxygen isotope zonation, the sulfosalt phase relations (discussed below) and the evidence for vapor-rich conditions at >455°C in a shallow, low-pressure environment indicate that the Fe-tennantite deposited from an expanding magmatic vapor as a high-temperature sulfosalt melt(S) that then cooled and crystallized. Symplectic textures (Fig. 6A) occur locally and may be interpreted (Mavrogenes *et al.* 2010) as the separation of excess Cu-Fe from the primary sulfosalt melt as the melt field shrank away from the starting composition (Fig. 9A,A′). Figure 5D shows a distinctive relationship between high and low Fe-tennantite that may indicate local melt immiscibility. Fe-tennantite is sometimes localized around euhedral and more complex quartz intergrowths (e.g., Figs 4B and 5E) in the manner of a wetting relationship (Figs 3F and 5E). Such wetting involving sulfosalt melts (as discussed below) has been demonstrated experimentally by Tomkins (2010).

Strikingly, the El Indio Copper Stage sulfide-quartz assemblages have no resemblance to the textures typically encountered in epithermal gold deposits that formed in paleo-geothermal systems where liquid water dominated at close to its liquid–vapor phase boundary. As noted below,

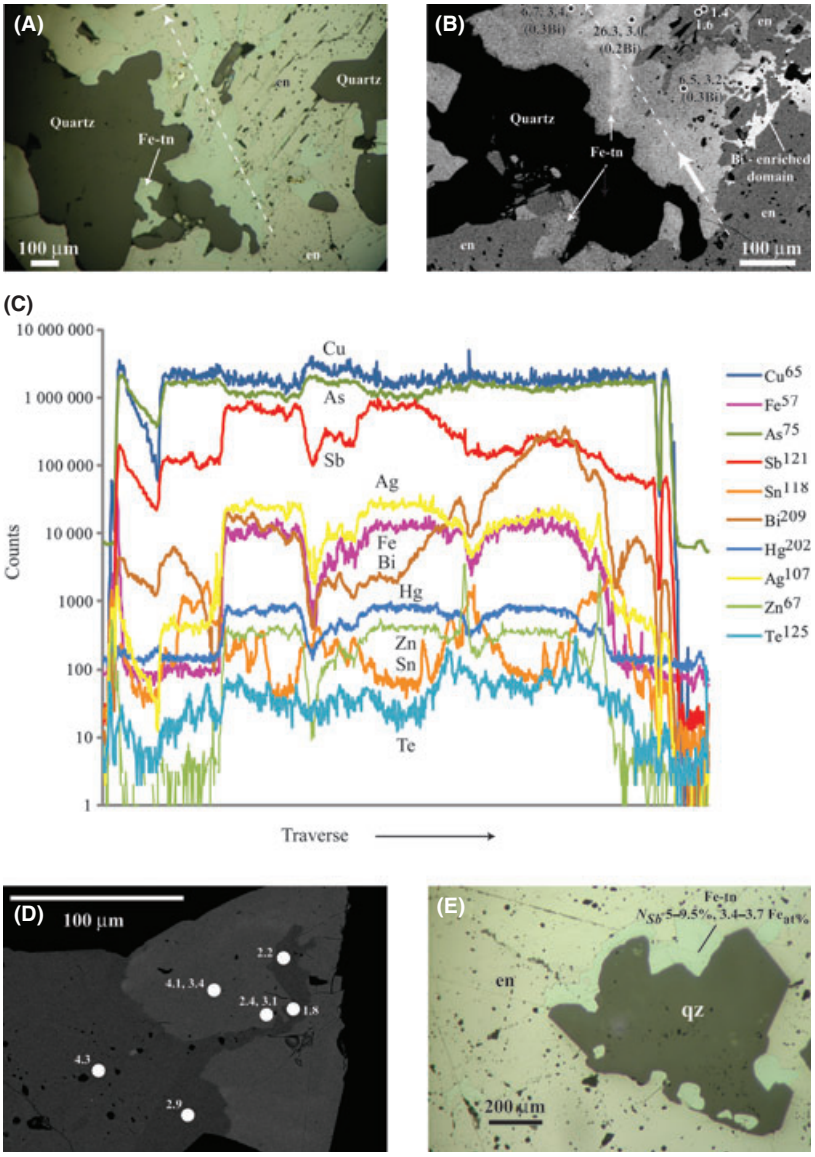

Fig. 5. (A,B) Relationships between enargite (with distinct cleavage), quartz with Fe-tennantite. Note the cryptic margin of replaced enargite that is clearly visible in reflected light (A) and the backscatter image (B). Analytical spot data shown as N_{Sb}, Fe (atom percent). Note zonation of the Fe-tennantite and the highly localized Bi-enrichment (see text). The dashed line is the laser ablation traverse whose data is shown in (C). (C) Laser ablation traverse (raw data, see text). (D) Intergrowth of low-Fe sulfosalt (N_{Sb} = 2.9–4.3) and lower N_{Sb} (1.8–4.1) sulfosalt in back scattered imagery, (E) Cluster of quartz crystals with a halo of low N_{Sb} Fe-tennantite inside vuggy enargite, visible in reflected light. Note the occlusion of Fe-tennantite by the quartz margin. Sample EI4216. En, enargite, Fe-tn, Fe-tennantite.

the pressure in the Copper Stage fractures and the intense prior wallrock alteration restricted groundwater entry to the expanding gas flow until reservoir pressures declined.

Phase relationships and heavy metal fractionation

Phase relations in the multicomponent tennantite-tetrahedrite solid solution series $[(Cu,Ag)_{10}(Fe, Cu)_2(Sb, As, Bi, Te)_4S_{13}]$ are poorly known but, by analogy with synthetic sulfosalt minerals used in the semiconductor industries, inevitably complex. To propose an integrated interpretation of the El Indio data, we here develop an empirical phase relation model based on the compositional relations detailed above and available experimental data for simpler systems. Stability relations for phases in the water-free ternary Cu-As-S system were determined experimentally by Maske & Skinner (1971) who demonstrated the extent of the sulfosalt melt phase relative to end-member tennantite (melting point 665°C, Fig. 9A, A′). Experimental data for the equivalent Cu-Sb-S system (Skinner *et al.* 1972) show that above 540°C, tetrahedrite melts to a similarly large compositional range. Tatsuka & Morimoto (1977) determined that the presence of iron at >1.72 atomic percentage increased the melting point of tetrahedrite by 12.7°C per atomic % iron. Our data contain 4–5 atomic % iron, suggesting a maximum increase in the melting point of Fe-tennantite of about 60°C. Assuming that the effects of trace components are negligible, as a first approximation, the system may be regarded as a binary solid solution between proxy end members – Fe-tennantite and Fe-tetrahedrite (Fig. 9B). However Maske & Skinner (1971) show that the stability field of tennantite expands relative to the field of melt immediately

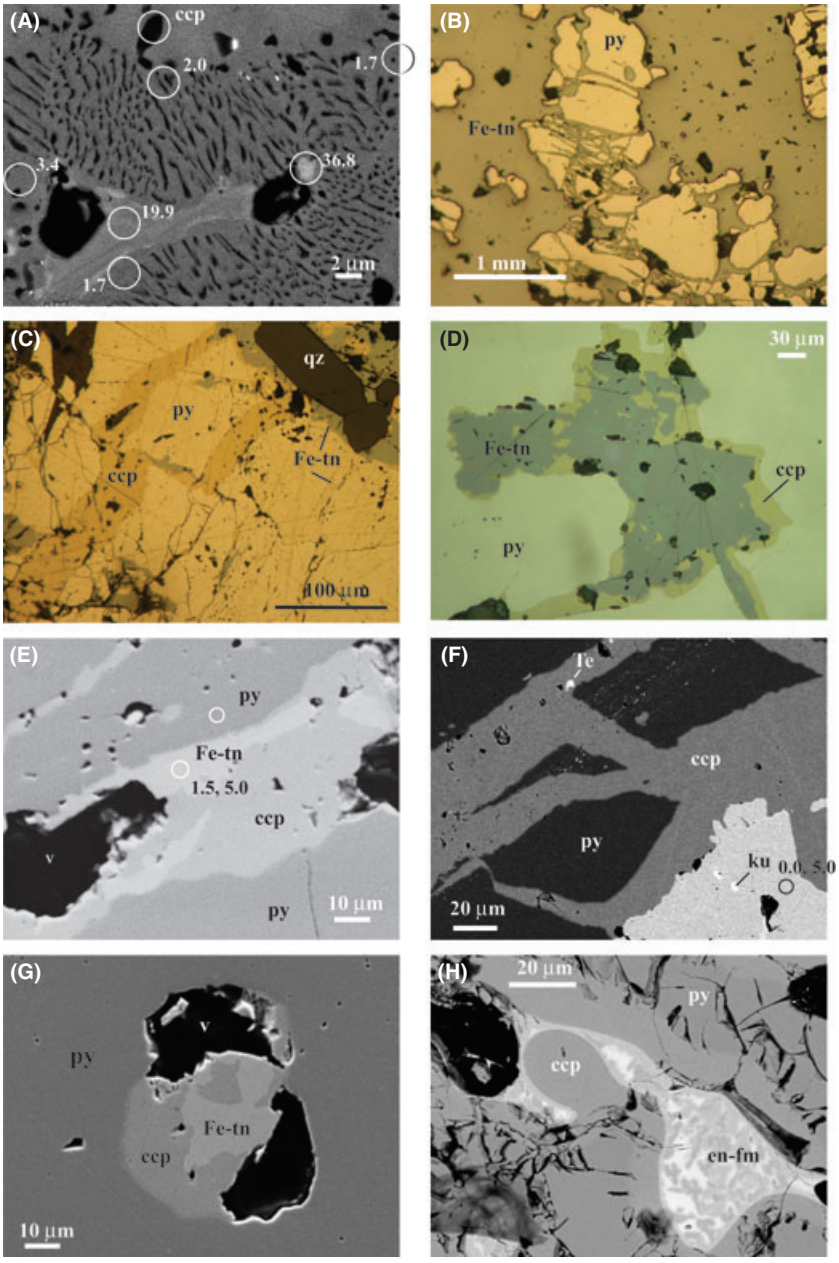

Fig. 6. Mineral intergrowths and replacement textures. (A) FESEM backscatter image showing symplectic Fe-tennantite (N_{Sb} = 2.0) – chalcopyrite intergrowth. Spot analyses with interaction diameter about 2 μm are shown as N_{Sb}. Note the presence of vugs and the intergranular space containing high Sb tennantite. Sample EI1285. (B) Fe-tennantite replacement of pyrite (py) to produce 'archipelago' texture. Sample EI1285, in reflected light. (C,D) chalcopyrite (ccp) and Fe-tennantite (Fe-tn) replacement of pyrite. Sample EI1300 reflected light. (E) chalcopyrite and Fe-tennantite replacement of pyrite. Note presence of vugs and infill textures. Sample EI1300 backscatter image with JEOLSEM analyses. (F) Progressive replacement of pyrite by chalcopyrite and Fe-tennantite. Note the trail of vugs and vug infills and the occurrence of bright heavy metal phases; Te indicates high Te in the spectrum and others indicate high Pb. ku is tentatively identified by analysis as kuramite, Cu_3SnS_4. Sample EI1300, backscatter image. (G) Fe-tennantite partially filling a vug in pyrite with the tennantite showing possible phase unmixing with the release of chalcopyrite. Sample EI1300, backscatter image. (H) experimental simulation of metastable chalcopyrite rim formation by tennantite (N_{Sb} = 25) by reaction with pyrite with development of interstitial symplectite in tennantite in the interstices; 2 days at 700°C (Bouma 2010).

below its melting point (665.5°C) so that here we include a solvus maximum (M) at about N_{Sb} = 10% but note that the original study took no account of the composition of any small fraction of vapor in the closed tube experiments. While the existence of M is not critical to the hypothesis developed here, we have presented some analytical data suggesting that fractionation toward low N_{Sb} values occurs locally. Sugaki *et al.* (1982) provided a limited range of experimental data for the Cu-As-Sb-S system and suggested a eutectic at about N_{Sb} = 70 ± 5% and 565°C. The El Indio data (and our unpublished data from other deposits) has an apparent upper N_{Sb} limit of approximately 77%, as discussed below, so that in Fig. 9B we have made provision for a eutectic (E), at about 600°C (allowing for the effect of iron in the structure).

The depositional sequence and reaction relationships at El Indio indicate trapping of Fe-tennantite melt in open space in fractured pyrite. The data presented here also indicate crystallization of enargite, postpyrite, as a solid phase that was *later* progressively dissolved by Fe-tennantite melt. These data then suggest that condensation of the Fe-tennantite melt from the vapor occurred at >665°C and <694°C (because crystalline enargite formed prior to Fe-tennantite) directly from magmatic vapor. By implica-

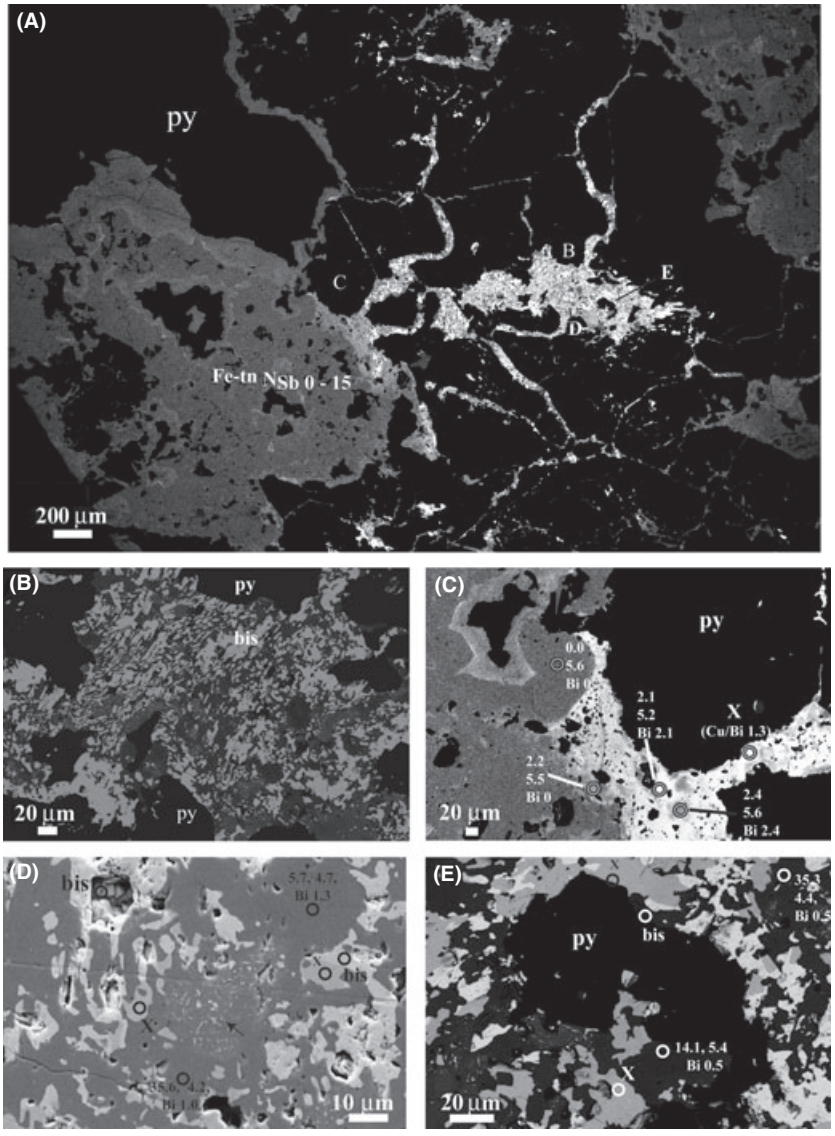

Fig. 7. (A) Localization of high bismuth domain in jigsaw fractured pyrite with diffusion-controlled zoning outward across earlier vuggy Fe-tennantite. 'B to E' indicate the location of the detailed images and analysis sets (B–E). (B) well developed fabric of bismuthinite + Fe-tennantite(lighter grey) corroding earlier pyrite(e) (26.8.10, SOI6), (C) 'reaction front' with Fe-tennantite (Bi = 2 to 2.4 atom percent Bi) + Cu-Bi phase X in contact with low N_{Sb} dark grey, Fe-tennantite (Bi < detection) that in turn is nucleated on vugs (analysis 9.09.10 SOI8). The Bi/(Cu + Bi) atomic ratio of phase X ranges from 44% to 49%. (D) intergrowth of bismuthinite (including in open vugs), and Fe-tennantite (Bi up to 1.3 at.percent). Arrow indicates exsolution intergrowth of bismuthinite and Fe-tennantite (N_{Sb} > 35%, 0.6–1.3 atomic percent Bi) (19.8.10, SOI2), (E) pyrite replacement by intergrowth of bismuthinite, Cu-Bi phase X and Fe-tennantite (26.8.10, SOI9). bis, bismuthinite, X, Cu-Bi phase X, py, pyrite and Fe-tennantite spot analyses designated by, for example, 2.2, 5.5, Bi 2.3, as N_{sb}, Fe, Bi (atom. percent).

tion, the deposition of crystalline pyrite occurred above this temperature but below the stability limit of pyrite (approximately 742°C). Simultaneous trapping of gas as vapor-filled vugs in Fe-tennantite is consistent with these data especially with the recognition of Cu_2S, sulfosalts and silica as discrete phases coating the inner surface of many vugs. The El Indio phase assemblages further suggest that silica hydrate co-deposited as a discrete immiscible phase[7] with the sulfosalt melt. Water released during subsequent dehydration mixed with vapor trapped during melt condensation and may be responsible for the evolution of the wide range of vug minerals that we have described in these assemblages.

The presence of vugs requires that consideration be given to the possible geometry of a vapor-melt relation ('vaporus') in the system Cu(Fe)-As-Sb-S. Figure 10 is a simplification of these more complex relations relative to the solid solution series assumed for Fe-tennantite to Fe-tetrahedrite in Fig. 9B. As very little is known about vapor-melt relations for sulfide or sulfosalt compositions, we assume for simplicity that the melt–vapor phase geometry is similar to that of the solidus-liquidus for the system.[8] The deposition of both crystalline pyrite and enargite from the vapor phase prior to the condensation of Fe-tennantite melt suggests that the vapor-melt phase boundary for this system lies below the melting point of enargite (Fig. 10).

[7]Experimental data and observations on magmatic sulfide deposits elsewhere indicate that sulfide melts may contain several percent water (Wykes & Mavrogenes 2005) that may in turn lower melting temperatures by a maximum of about 35°C.

[8]Hansen & Aderko (1958, p.177) show an analogous vaporus–melt phase relationship in the system As-S up to >700°C.

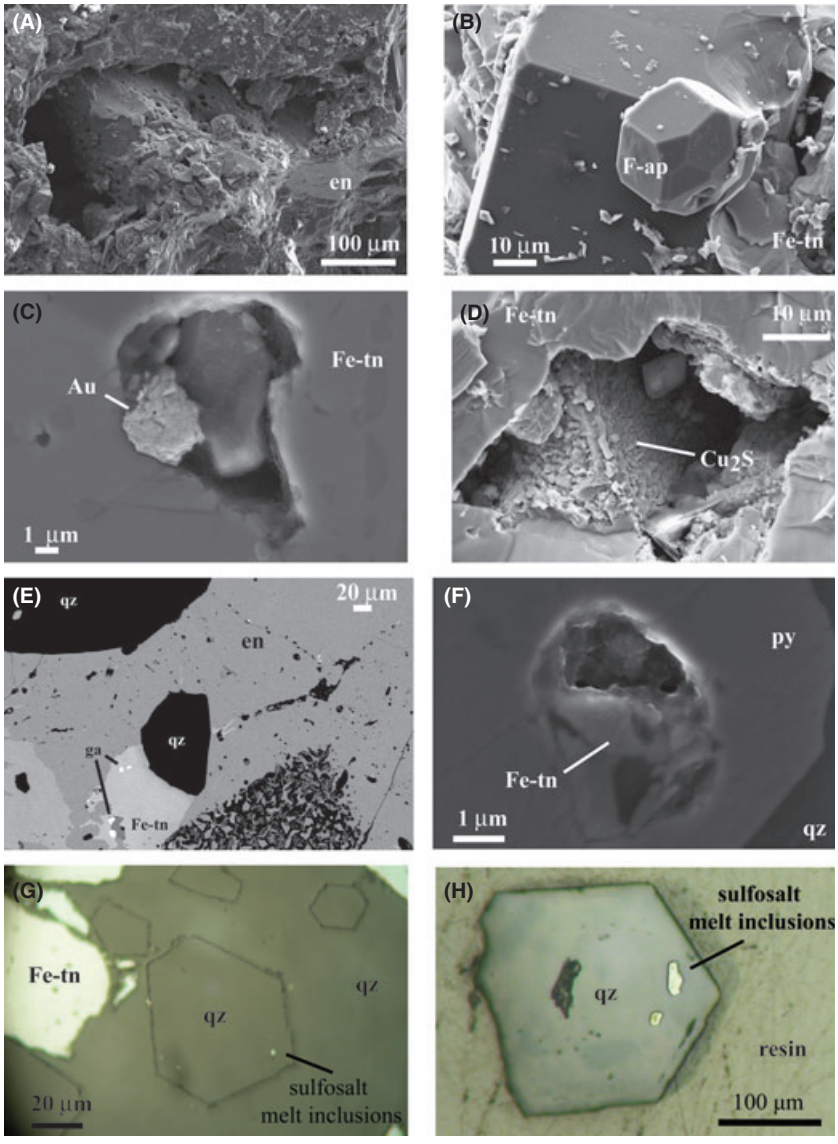

Fig. 8. Vugs and mineral inclusions. (A) Large and small vugs typical of the broken surfaces of the El Indio samples, en, enargite; EI1300a, (B) euhedral fluorapatite (F-ap) crystals in a cavity in Fe-tennantite (Fe-tn), EI1300, (C) cluster of gold crystals (Au) in a vug in Fe-tennantite, EI1300T, (D) Cu_2S lining a vug in Fe-tennantite, EI4268, (E) inclusions or vug fillings of galena, ga, in Fe-tn (N_{Sb}13.1%, Fe 3.9, 1.4%Bi), adjacent to laser ablation track, EI4216 (cf Fig. 5C), (F) sulfosalt inclusion (unmixed sulfosalts providing a spot analysis (approximately 2 μm) of N_{Sb} = 11%) inside a pyrite inclusion in a euhedral quartz crystal, EI1300T, (G) Intergrowth of quartz and Fe-tennantite; note the discrete hexagonal quartz crystals growing within the quartz mass, EI4216FIB (cf. Fig. 5), (H) Euhedral quartz (EI1285, 7524), showing primary sulfide/sulfosalt melt inclusions. (A–D) and (F) are secondary electron images on fractured surfaces, (E) is a back scattered image, and G–H are reflected light images. The hatchured area in (E) is the termination of a laser ablation track.

The bulk concentrate mined from El Indio had an N_{Sb} of 2.9% (Balaz *et al.* 2000) and contained about 45 wt% enargite. The most abundant Fe-tennantite composition in the El Indio sample suite also limits the antimony content of the initial melt to N_{Sb} approximately 5%, with the content of other metals and semi-metals <0.2 wt%). The fractionation of high N_{Sb} zoned Fe-tennantite further suggests that the N_{Sb} of the magmatic vapor phase (V_0) was higher than that of the bulk mined concentrate and in the vicinity of the average crustal abundance ratio for granite and basalt (N_{Sb} = 7.6 and 5.8% respectively). The El Indio data show that during fractionation the sulfosalt melt composition became enriched in antimony and the N_{Sb} for the crystallizing sulfosalt increased to a maximum of 77%, suggesting a system eutectic (Fig. 10).

Sb, Bi and Te are the principal substituents for As in the X site of the standard tennantite formula of Moelo *et al.* (2008). Assuming that for large-ion Group 5A (*syn.* Group 15) heavy metals that metal-sulfur bond energies are similar, the principal steric control on semi-metal substitution into crystalline tennantite is bond length. It is then a reasonable assumption that partitioning between weakly structured melt and vapor should similarly reflect relative bond lengths because the electron configurations of the large heavy metal ions result in similar vapor phase speciation. Our data show that the concentrations of bismuth and tellurium generally remain below detection until the Fe-tennantite composition reaches N_{Sb} > 20(B in Fig. 10). At N_{Sb} approximately 20, 80% of the original arsenic in the vapor has crystallized with commensurate increase in the melt concentration of other metals. In turn,

the vapor (derived from silica hydrate dehydration) associated with the melt also fractionates and becomes enriched in heavy metals (Fig. 10) in a sequence consequent on their respective metal–sulfur bond distances (Table 2).[9] We suggest that it is this process that leads to the evolution of the composition of the vapor phase and results in the wide range of discrete heavy metal vug minerals as well as incompatible phases such as aluminosilicates and fluorapatite. The late release of vapor enriched in bismuth through new cracks in the pyrite results in the localized complex bismuth assemblages (Fig. 7).

Bismuth has received attention as a potential *flux* that reduces the melting point of sulfides such as galena (Tomkins *et al.* 2007). The great majority of Fe-tennantite analyses in the El Indio suite have bismuth contents below FESEM detection (approximately 0.1 wt %), indicating that bismuth is a trace element[10] in the primary sulfosalt melt with a potential to lower the melting point by at most a few degrees. However, despite the low concentration of bismuth, domains of bismuth enrichment occur locally within fractured pyrite and enargite (Figs 5B and 7A) and appear to have developed by diffusion into adjacent preexisting Fe-tennantite. Figure 9C reproduces the experimental data of Sugaki & Shima (1972) for the system Cu_2S-Bi_2S_3 and includes the range of compositions for the $(CuBi)_{1-y}S_2$ phase that appears to be in equilibrium with Bi_2S_3 and Bi-substituted Fe-tennantite. These data, again noting the occurrence of Cu_2S in coexisting vugs, indicate phase unmixing from melt above 650°C in the presence of vapor. A complex mix of bismuthinite and $(CuBi)_{1-y}S_2$ occurs with Fe-tennantite (N_{Sb} = 50.9, Bi = 1.3 atomic %) as a discrete zone in fractured pyrite (Fig. 7A). The precursor to this assemblage was highly reactive to pyrite and consumed earlier lower N_{Sb} Fe-tennantite (Fig. 7D,E). The localization of the bismuthinite-$(CuBi)_{1-y}S_2$ assemblage by fractured pyrite and enargite indicates that a bismuth-rich vapor phase evolved during cooling of the assemblage moved through fractures in the pyrite and reacted with the Fe-tennantite such that concomitant enrichment in bismuth to more than 1.3 atomic % enabled formation of Cu-Bi-S minerals.

Far-from-equilibrium chemical reactions

None of the textural or compositional relationships preserved in the El Indio suite may be interpreted as having

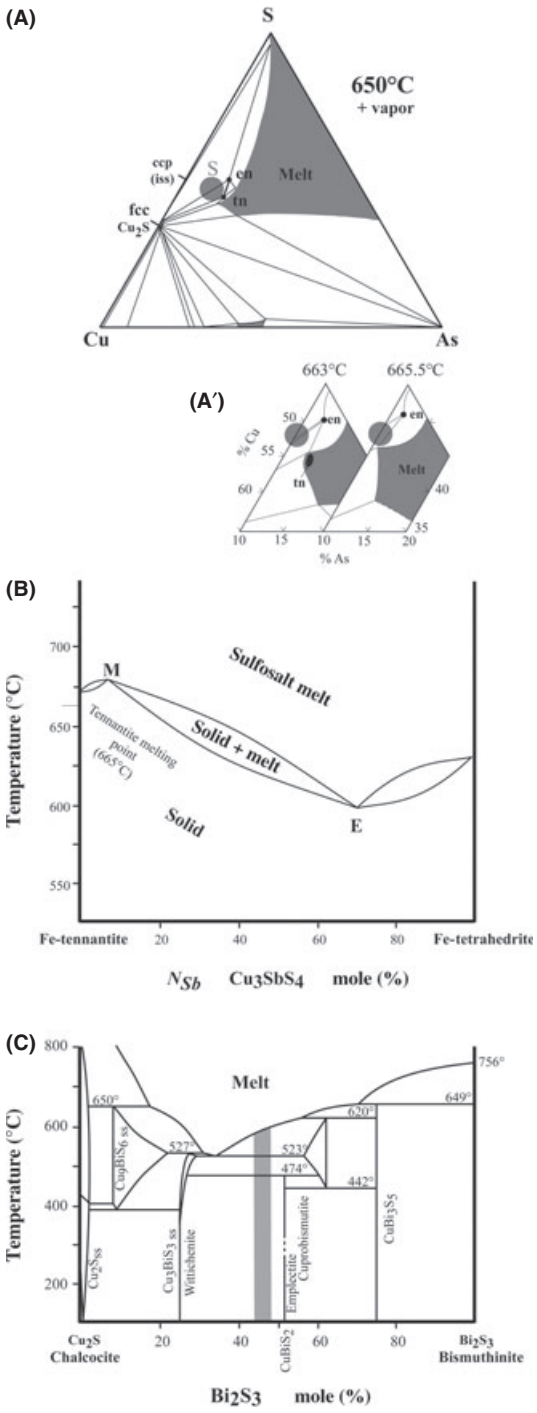

Fig. 9. (A, A′) Phase relations in the system Cu-As-S between 663 and 650°C (from Maske & Skinner 1971) showing the rapid change in the extent of the sulfosalt melt field over a small temperature range and the isolated tennantite composition just prior to melting; (B) empirical phase relations for the tennantite-tetrahedrite solid solution series (see text), (C) Phase relations in the system $Cu_2SBi_2S_3$ (Sugaki & Shima 1972) showing the range of $CuBi_1$-yS_2 compositions from sample EI1285 (Fig. 7B–D).

[9]A similar pattern of heavy metal fractionation has been described by Helmy *et al.* (2010) for experiments involving sulfide melts and monosulfide solid solution in the context of magmatic sulfide deposits.

[10]At El Indio, the bismuth concentration of mined pyrite-sulfosalt concentrates is about 0.1%, which translates into 0.2 atom percent relative to total antimony and arsenic.

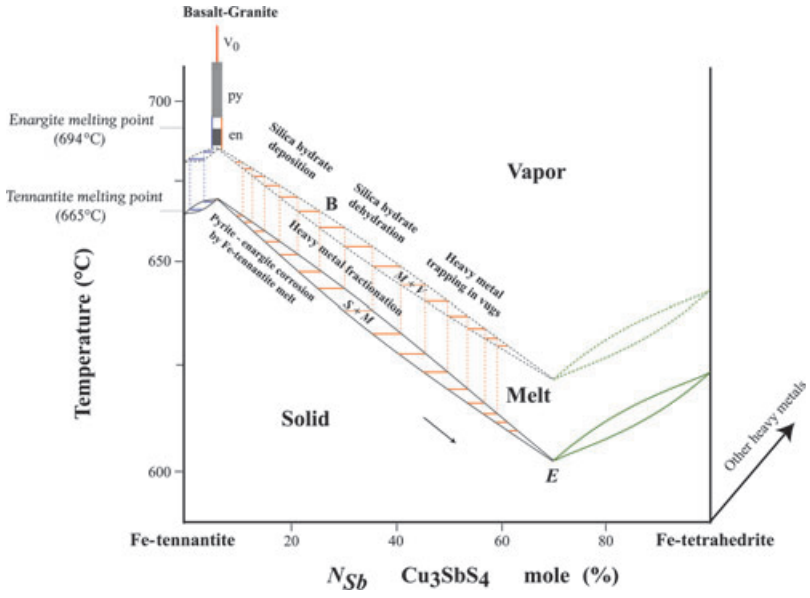

Fig. 10. Synthesis of sulfide-sulfosalt deposition and fractionation sequence in the system Cu-Fe-As-Sb-S – heavy metals as discussed in the text. Melting point of enargite from Muller & Blachnik (2002).

Table 2 Relative metal–sulfur bond distance in crystalline solids (calculated from the data of Brese & O'Keeffe 1991) with respect to the structural site in tennantite (see text). R^3 is the cube of the bond distance relative to the As–S bond expressed as a percent to illustrate the size difference of ions in a substitution relationship. For comparison, bond distance parameters are also shown for selected other heavy metals.

Element	Bond valence parameter	Tennantite structural site	Atomic weight	R^3 (%)
Cu	1.86	B	63.55	
Ag	2.15	B	107.87	
Zn	2.09	C	65.37	
Fe	2.16	C	55.85	
Mn	2.20	C	54.94	
Cd	2.29	C	112.4	
Hg	2.32	C	200.59	
As	2.26	X	74.92	
Sb	2.45	X	121.75	27
Sn	2.45	X	118.69	27
Te	2.45	X	127.6	27
Bi	2.55	X	208.98	44
S	2.07		32.06	
Au	2.03		196.97	
Se	2.25		78.96	
Mo	2.35		95.94	
Re	2.37		186.2	
Tl	2.63		204.37	
Pb	2.78		207.2	

formed in a close-to-equilibrium state. The diffusion-controlled replacement of pyrite and enargite by Fe-tennantite and the localization of bismuth-rich assemblages clearly indicate a far-from-equilibrium chemical environment (Henley & Berger 2000) resulting from the throttling of magmatic vapor from high to low pressure in the fracture array. This arises because the vapor phase solubilities of metals as well as the speciation of major components such as alkali chlorides and silica are strongly pressure-dependent (Henley & Berger 2011). Because the principal solvent interaction is the weak bonding between, for example, $CuCl_{2,g}$ and H_2O_g, in the form of $CuCl_2{,}nH_2O_g$ clusters (or equivalent sulfide species), changes in the activity of water during expansion are critical controls on the vapor phase solubility of sulfides and sulfosalts. Arsenic as arsenic sulfide or hydroxide vapor species (Pokrovski *et al.* 2005) are similarly victims of expansion and rapidly react with other destabilized metal species to deposit complex sulfosalt minerals. Even though experimental data are not available for metal species in volcanic gases, it is clear that as magmatic vapor expands within a fracture network, rapid changes in the total vapor pressure inevitably establish far-from-equilibrium depositional conditions, in turn setting in train the solid-melt-vapor fractionation processes preserved at El Indio. The aggressive replacement of pyrite and enargite by Fe-tennantite, as discussed below, is a prime example.

In a far-from-equilibrium environment, fast reactions yield products that are subsequently unstable and the resultant intermediate assemblages continue to react toward an equilibrium or stationery state. However, their progress is limited by, for example, the relative diffusion rates of the species involved, resulting in incomplete replacement and preservation of remnants of the intermediate phases. In the El Indio assemblages described here, chalcopyrite is preserved as an intermediate product of the replacement of pyrite by Fe-tennantite and sometimes forms discrete veins through pyrite. These remnants of the reaction sequences suggest that both pyrite and enargite crystallized rapidly from the vapor phase but were unstable with respect to Fe-tennantite melt. Subsequently, the early-fractionated Fe-tennantite was unstable with respect

to the bismuth-enriched vapor (that evolved during Fe-tennantite fractionation of the heavy metals) through new cracks in the remaining brittle pyrite and enargite.

Coupled substitution reactions

A number of secondary processes attend the interaction of sulfosalt melt with earlier crystalline phases. Fe-tennantite melt aggressively corrodes and replaces both pyrite and enargite (Figs 5 and 6). The detail shown in Fig. 6 indicates that the reaction proceeds by initial pitting of the pyrite by reacting with vapor followed by a reaction sequence through chalcopyrite to Fe-tennantite. The presence of isolated heavy metal inclusions, including Te and Sn minerals, and the LA-ICP-MS data (Fig. 5) show that this reaction introduced a wide range of elements not present in the early pyrite or enargite and therefore indicates that the reaction was not simply a response to changing activity of sulfur species. Preservation of cryptic crystal outlines (Fig. 5B) shows that the sequence of coupled substitution and electron transfer reactions (c.f. Renock 2010) occurred by diffusion. The solid state replacement of enargite involves electron transfer (As^{V} to As^{III}) coupled with substitution by Sb^{III} and other trace semi-metals and partial exchange of Cu^{II} by Fe into the structure as Fe^{II}, Fe^{III}, and $Fe^{II/III}$ (Makovicky *et al*. 1990). Blanchard *et al*. (2007) suggest that arsenic substitution in pyrite occurs by replacement of sulfur in the unit cell. An association with vugs, some containing Cu_2S, suggests the release of a secondary vapor phase during these reactions. The pyrite-Fe-tennantite reaction involves inward diffusion of Cu^{I} and As^{III} probably kinetically controlled by vacancies in the pyrite (Birkholz *et al*. 1991) with a counter diffusion of Fe resulting in $CuFeS_2$, with Fe as Fe^{III} (Pearce *et al*. 2006), as an intermediate phase forming rims and discrete veins. Figure 6H shows an experimental simulation of the reaction pyrite + tennantite ($N_{Sb} = 25$) (Bouma 2010) at 700°C with pyrite reacting rapidly with the tennantite melt to produce a well-defined metastable rim of $CuFeS_2$ within 48 h.

The replacement of early pyrite by sulfosalts is common to high-sulfidation deposits worldwide. It is further documented for sulfide–sulfosalt assemblages at the Chinkuashih deposit, Taiwan, where subsolfatara mineralization is preserved to about 1500 m below the original surface (R. Henley, B. Berger, unpublished data) and the replacement reaction is shown to be pressure-dependent, with lower pressures favoring sulfosalts.

SYNTHESIS

Figure 1 posed a number of questions. How were fractures developed through the pre-existing pyrite and how was open space created within which the complex '*porphyritic*' tennantite-quartz assemblages developed? How were the components of the sulfosalts (Cu, Fe, As, Sb, S, ±Te, Ag, Bi, Tl, Sn) transported into this space along with silica? How may we account for the occurrence of discrete sulfide (e.g., galena and other heavy metal sulfides), sulfosalt minerals, and tiny gold crystal clusters in some vugs while others are empty? The data presented here indicate that magmatic vapor expansion through the controlling fault array of the El Indio fumarole-vent system was a consequence of on-going crustal stress that opened a network of cracks and dilatations. Vapor expansion first deposited pyrite at about 700°C in this newly opened fracture space. The fracture array remained under stress with subsequent fracturing of the early pyrite and the switch to the deposition of enargite and subsequent condensation of a multicomponent, low-viscosity (Dobson *et al*. 2000) sulfosalt melt containing dispersed silica hydrate at >675°C. The composite sulfosalt melt flowed through fractures into available dilatations with aggressive corrosion and dissolution of the earlier pyrite and enargite (Figs 5 and 6). The sulfosalt melt then crystallized, as described below, to produce the complex zoned Fe-tennantite and discrete heavy metal inclusions (Fig. 3 and 4). During melt crystallization, the dispersed hydrated silica coalesced progressively and crystallized to euhedral quartz with entraped melt inclusions (Fig. 8G,H) and sequential release of water. Trace element partitioning between this released water and fractionating sulfosalt melt resulted in the abundant mineralized vugs and the wide range of heavy metal inclusions in the Fe-tennantite, including gold (Fig. 8A–F).

Interestingly, the cross-cutting 'Gold Stage' chalcedonic silica veins[11] (Jannas 1995) are characterized by a geochemically more complex suite of sulfides and sulfosalts than the Copper Stage, including tungstates, silver, lead and bismuth sulfides, tellurides, and gold (Fig. 2). As described above, these elements are also present within the earlier Fe-tennantite assemblages where clearly defined zonation and abundant vugs indicate heavy metal fractionation between the solid, the contiguous melt and vapor phases. It is possible, and permitted by the oxygen and deuterium isotope data of Jannas *et al*. (1999), that this distinctive phase of mineralization is a lower pressure phenomenon related to the mixing of evolved heavy metal-enriched vapor and groundwater in available fractures as pressure in the magmatic vapor reservoir decreased as a result of discharge.

Vapor phase geochemical processes in active fumaroles

The sulfide–sulfosalt assemblages preserved in the fracture system at El Indio around one thousand meters below the paleo-surface provide insights to the processes occurring in

[11]The fluid inclusion data reported by Jannas (1995) are primarily from the secondary quartz within the recrystallized silica in these veins.

modern active volcanoes. While enargite and tennantite are found in pumice on Popacatapetl, Mexico (Larocque *et al.* 2008), arsenic minerals are rare in fumarole sublimates except as complex sulfosalts such as vurroite, $Pb_{20}Sn_2(Bi,As)_{22}S_{54}Cl_6$ in association with other rare complex sulfosalts such as lillianite $Pb_{2.88}Bi_{2.12}(S_{5.67}Se_{0.33})S_6$ and galenobismutite, $Pb_3Bi_2S_6$ (e.g., Garavelli *et al.* 2005, Pinto *et al.* 2006) at, for example, Vulcano, Italy, and Kudriavy, Kurile Islands. Similarly, antimony minerals are seldom observed in fumarole sublimates or encrustations although Africano *et al.* (2002, 2003) have shown that both As and Sb are enriched in altered rocks adjacent to fumarole vents. Because the deposition of enargite and Fe-tennantite in the El Indio paleo-fumarole requires that the expanding magmatic vapor becomes depleted in arsenic and relatively enriched in heavier metals, a similar vertical separation of heavy metals may be occurring in these active fumaroles.

Williams-Jones *et al.* (2002) reviewed and summarized a limited range of metals for fumarolic discharges from andesitic to felsic volcanoes. We are here only concerned with high-temperature fumaroles with exit temperatures above 600°C with minimal interaction with external groundwater or cold magmatic vapor condensate. With the exception of Mount St. Augustine, Alaska (870°C, 33 mg kg^{-1}), the reviewed arsenic concentrations were well below 4.5 mg kg^{-1}. Low arsenic concentrations are also confirmed by the data of Signorelli (1997) with the only exceptions in his data set being Vulcano (625°C, 30 mg kg^{-1}) and Galeras, Colombia (642°C, 15 mg kg^{-1}). Antimony analyses are not commonly reported for fumarole condensate samples perhaps because of very low values. In the data tabulated by Williams-Jones *et al.* (2002), antimony concentrations range from 0.01 to 0.5 mg kg^{-1} giving an N_{Sb} range for the gas discharges of 0.4–26.[12]

This contrast between the subsurface arsenic-rich sulfosalt assemblages described at El Indio 900 m or so below the surface of a paleo-solfatara and the arsenic-poor sublimates and vapor discharges observed in modern fumarole vents and sampling tubes highlights the problem that gas samples taken at surface close to atmospheric pressure are potentially depleted in metals because of subsurface deposition during expansion from higher pressures. We suggest that this contrast arises because some 90% or more of the arsenic in a magmatic gas is deposited subsurface along with antimony. The ratio of the volume of quartz to tennantite shown in Fig. 1 is about 30% and is equivalent to a SiO_2/As mole ratio of about 1.5, because the solubility of silica in a low-density vapor is around 3000 mg kg^{-1} (Manning 1994) at magmatic temperatures. Assuming quantitative deposition of both silica and arsenic, the original arsenic concentration of the magmatic vapor would therefore have been about 2000 mg kg^{-1}.[13] In present-day fumaroles, most of this arsenic is probably also deposited subsurface in response to vapor expansion or is dispersed by vapor condensation into groundwater that flows away from the volcanic center and potentially constitutes a health hazard in some districts. Similarly, the primary vapor concentration of antimony would be around 200 mg kg^{-1}. The common occurrence of bismuth sulfosalts around active fumaroles also suggests enrichment of the vapor phase in bismuth as well as other heavy metals as a consequence the of subsurface fractionation of As-Sb sulfosalts as described here.[14] Likewise, the 'metallic snow' observed on Maxwell Montes in the Venusian Highlands (Schaefer & Fegley 2004) may directly or indirectly be attributed to similar vapor expansion processes.

ACKNOWLEDGEMENTS

We thank Frank Brink for his patience while we explored the micron-scale world revealed by FESEM. We thank Andy Christie and Barney Berger for invaluable discussion and Francois Robert for arranging the sample suite from El Indio. We especially appreciated the thoughtful and constructive comments provided by Andy Tomkins, Steve Kesler, Paul Barton (Jr) and Phil Bethke, and assistance from Nigel Richardson and Kirsty Vincent.

REFERENCES

Africano F, van Rompaey G, Bernard A, Le Guern F (2002) Deposition of trace elements from high temperature gases at Satsuma-Iwojima volcano. *Earth Planet Space*, **54**, 275–86.

Africano F, Bernard A, Korzhinsky M (2003) High temperature volcanic gas geochemistry (major and minor elements, at Kudryavy volcano, Iterup Island, Kurile Arc, Russia. *Vulcanica*, **1**, 87–94.

[12]Occurrences of enargite in crater lakes such as Kawah Ijen, Indonesia (Delmelle & Bernard 1994), are relatively common but represent a quite different set of processes with accumulation of highly soluble arsenic into cooler water. The same overall process is responsible for high concentrations of arsenic in groundwaters flanking active volcanoes (Signorelli *et al.* 1998).

[13]Since magmatic vapor expands through the basement, commonly sedimentary, rocks beneath volcanoes prior to discharging through fractures, it is possible that much of the arsenic and antimony are distilled from these rocks rather than derived directly from magma.

[14]The gold and tellurium precipitated in fumarole vents at Vulcano (Fulignati & Sbrana 1998) and Colima, Mexico (Taran *et al.* 2000), may evidence heavy metal fractionation of the vapor phase and condensation into groundwater (or high level liquid condensate) in the same way that at El Indio the late gold-rich stage (*post* the assemblages discussed in this paper) is distinguished by a range of heavy metal sulfides and sulfosalts together with gold and silver minerals within chalcedonic silica whose stable isotope composition indicates substantial groundwater mixing.

Balaz P, Achimovicov M, Bastl Z, Ohtani T, Sanchez M (2000) Influence of mechanical activation on the alkaline leaching of enargite concentrate. *Hydrometallurgy*, **54**, 205–16.

Berger BR, Henley RW (2011) Magmatic-vapor expansion and the formation of high-sulfidation gold deposits: structural controls on hydrothermal alteration and ore mineralization. *Ore Geology Reviews*, **39**, 75–90.

Bethke PM, Rye RO, Stoffregen RE, Vikre PG (2005) Evolution of the magmatic-hydrothermal acid-sulfate system at Summitville, Colorado: integration of geological, stable-isotope, and fluid-inclusion evidence. *Chemical Geology*, **215**, 281–315.

Birkholz M, Fiechter S, Hartmann A, Tributsch H (1991) Sulfur deficiency in iron pyrite (FeS_{2-x}) and its consequences for band structure models. *Physical Review B*, **43**, 11926–36.

Blanchard M, Alfredsson MJ, Wright K, Catlow CRA (2007) Arsenic incorporation into FeS_2 pyrite and its influence on dissolution: a DFT study. *Geochimica et Cosmochimica Acta*, **71**, 624–30.

Botcharnikov RE, Shmulovich KI, Tkachenko SI, Korzhinsky MA, Rybin AV (2003) Hydrogen isotope geochemistry and heat balance of a fumarolic system: Kudriavy volcano, Kuriles. *Journal of Volcanology and Geothermal Research*, **124**, 45–66.

Bouma M (2010) *The Cu-As-Sb-Fe-S Sulfosalts: Phase Relations in Experimental and Natural Systems.* Honours thesis, Australian National University, 88 p. (unpublished)

Brese NE, O'Keeffe M (1991) Bond-valence parameters for solids. *Acta Crystalographica*, **47**, 192–7.

Chouinard A, Williams-Jones AE, Leonardson RW, Hodgson CJ, Silva P, Tellez JV, Rojas F (2005) Geology and genesis of the multistage high-sulfidation epithermal Pascua Au-Ag-Cu deposit, Chile and Argentina. *Economic Geology*, **100**, 463–90.

Delmelle P, Bernard A (1994) Geochemistry, mineralogy, and chemical modeling of the acid crater lake of Kawah Ijen Volcano,Indonesia. *Geochimica et Cosmochimica Acta*, **58**, 2445–60.

Deyell CL, Bissig T, Rye RO (2004) Isotopic evidence for magmatic-dominated epithermal processes in the El Indio-Pascua Au-Cu-Ag Belt and relationship to geomorphologic setting. *Society of Economic Geologists Special Publication*, **11**, 55–73.

Deyell CL, Leonardson R, Rye RO, Thompson JFH, Bissig T, Cooke DR (2005) Alunite in the Pascua-Lama high-sulfidation deposit: constraints on alteration and ore deposition using stable isotope geochemistry. *Economic Geology*, **100**, 131–48.

Dobson DP, Crichton WA, Vocaldo L, Jones AP, Wang Y, Uchid T, River M, Sutton S, Brodhol JP (2000) In situ measurement of viscosity of liquids in the Fe-FeS system at high pressures and temperatures. *American Mineralogist*, **85**, 1838–42.

Fulignati P, Sbrana A (1998) Presence of native gold and tellurium in the active high-sulfidation hydrothermal system of the La Fossa volcano, Vulcano, Italy. *Journal of Volcanology and Geothermal Research*, **86**, 187–98.

Garavelli A, Mozgova NN, Orlandi P, Bonaccorsi E, Pinto D, Moëlo Y, Borodaev YS (2005) Rare sulfosalts from Vulcano, Aeolian Islands, Italy. VI., Vurroite, Pb20Sn2(Bi,As)22S54Cl6, a new mineral species. *Canadian Mineralogist*, **43**, 703–11.

Hansen M, Aderko K (1958) *Constitution of Binary Alloys*, p. 1305. McGraw-Hill, New York.

Helmy HM, Ballhaus C, Wohlgemuth-Ueberwasser C, Fonseca ROC, Laurenz V (2010) Partitioning of Se, As, Sb, Te and Bi between monosulfide solid solution and sulfide melt – application to magmatic sulfide deposits. *Geochimica et Cosmochimica Acta*, **74**, 6174–9.

Henley RW, Berger BR (2000) Self-ordering and complexity in epizonal mineral deposits. *Annual Reviews of Earth and Planetary Sciences*, **28**, 669–719.

Henley RW, Berger BR (2011) Magmatic-vapor expansion and the formation of high-sulfidation gold deposits: chemical controls on alteration and mineralization. *Ore Geology Reviews*, **39**, 63–74.

Henley RW, Stewart MK (1983) Chemical and isotopic changes in the hydrology of the Tauhara geothermal field due to exploitation at Wairakei. *Journal of Volcanology and Geothermal Research*, **15**, 285–314.

Jannas RR (1995) *Reduced and Oxidizing High Sulfidation Deposits of the El Indio District, Chile.* Ph.D. dissertation, p. 421. Harvard University, Cambridge.

Jannas RR, Beane RE, Ahler BA, Brosnahan DR (1990) Gold and copper mineralization at the El Indio deposit, Chile. *Journal of Geochemical Exploration*, **36**, 233–66.

Jannas RR, Bowers TS, Petersen U, Beane RE (1999) High-sulfidation deposit types in the El Indio district, Chile. In: *Geology and Ore Deposits of the Central Andes* (ed. Skinner BJ), pp. 219–66. Society of Economic Geologists Special Publication, *7*.

Larocque ACL, Stima JA, Siebe C, Greengrass K, Chapman R, Mejia SR (2008) Deposition of a high-sulfidation Au assemblage from a magmatic volatile phase, Volcán Popocatépetl, Mexico. *Journal of Volcanology and Geothermal Research*, **170**, 51–60.

Makovicky E, Karup-Møller S (1994) Exploratory studies on substitution of minor elements in synthetic tetrahedrite. I. Substitution by Fe, Zn, Co, Ni, Mn, Cr, V and Pb. Unit cell parameter changes on substitution and the structural role of "Cu^{2+}". *Neues Jahrb. Mineral., Abh.*, **167**, 89–123.

Makovicky E, Forcher K, Lottermoser W, Amthauer G (1990) The Role of Fe^{2+} and F^{3+} in Synthetic Fe-substituted Tetrahedrite. *Mineralogy and Petrology*, **43**, 73–81.

Manning CE (1994) The solubility of quartz in H_20 in the lower crust and upper mantle. *Geochimica et Cosmochimica Acta*, **58**, 4831–9.

Maske S, Skinner BJ (1971) Studies of the sulfosalts of copper I. Phases and phase relations in the system Cu-As-S. *Economic Geology*, **66**, 901–18.

Mavrogenes J, Henley RW, Reyes A, Berger BR (2010) Sulfosalt melts: evidence of high-temperature gas transport of metals in the formation of high-sulfidation lode gold deposits. *Economic Geology*, **105**, 257–62.

Moelo Y, Makovicky E, Mozgova NN, Jambor JL, Cook N, Pring A, Paar W, Nicke EH, Graeser S, Karup-Mølle S, Balić-Žunić T, Mumme WG, Vur F, Topa D, Bindi L, Bent K, Shimizu M (2008) Sulfosalt systematics: a review. Report of the sulfosalt sub-committee of the IMA Commission on Ore Mineralogy. *Journal of Mineral*, **20**, 7–46.

Muller A, Blachnik R (2002) Reactivity in the system copper–arsenic–sulfur, I. The formation of Cu3AsS4, enargite. *Thermochimica Acta*, **387**, 153–71.

Nuccio PM, Paonita A, Sortino F (1999) Geochemical modeling of mixing between magmatic and hydrothermal gases: the case of Vulcano Island, Italy. *Earth and Planetary Science Letters*, **167**, 321–33.

Pearce CI, Pattrick RAD, Vaughan DJ, Henderson CMB, van der Laan G (2006) Copper oxidation state in *chalcopyrite*: mixed Cu d^9 and d^{10} characteristics. *Geochimica et Cosmochimica Acta*, **70**, 4635–42.

Pinto D, Balic-Zunik T, Garavelli A, Makovicky E, Vurro F (2006) Comparative crystal-structure study of Ag-free lillianite and galenobismutite from Vulcano, Aeolian islands, Italy. *Canadian Mineralogist*, **44**, 159–75.

Pokrovski GS, Zakirov IV, Roux J, Testemale D, Hazemann J-L, Bychkov AY, Golikova GV (2005) Experimental study of arsenic speciation in vapor phase to 500° C: implications for

As transport and fractionation in low-density crustal fluids and volcanic gases. *Geochimica et Cosmochimica Acta*, **66**, 3453–80.

Renock DJ (2010) Redox processes in sulfide minerals, PhD thesis. University of Michigan, p. 183.

Rye RO (2005) A review of the stable-isotope geochemistry of sulfate minerals in selected igneous environments and related hydrothermal systems. *Chemical Geology*, **215**, 5–36.

Schaefer L, Fegley B (2004) Heavy metal frost on Venus. *Icarus*, **168**, 215–9.

Signorelli S (1997) Arsenic in volcanic gases. *Environmental Geology*, **32**, 239–44.

Signorelli S, Buccianti A, Martini M, Piccardi G (1998) Arsenic in fumarolic gases of Vulcano (AeolianIslands,Italy) from 1978to 1993: geochemical evidence from multivariate analysis. *Geochemical Journal*, **32**, 367–82.

Skinner BJ, Luce D, Makovick E (1972) Studies of the sulfosalts of copper, III, Phases and phase relations in the system Cu-Sb-S. *Economic Geology*, **67**, 924–38.

Sugaki A, Shima J (1972) Phase relations of the Cu_2S-Bi_2S_3 system. *Yamaguchi University for Technical Report*, **1**, 45–70.

Sugaki A, Kitakaze A, Shimizu Y (1982) Phase relations in the Cu_3AsS_4-Cu_3SbS_4 join. *Science Reports of the Tohoku University*, 3rd Series, **XV**, 257–71.

Taran YA, Bernard A, Gavilanes J-C, Africano F (2000) Native gold in mineral precipitants from high temperature volcanic gases of Colima volcano, Mexico. *Applied Geochemistry*, **15**, 337–46.

Tatsuka K, Morimoto N (1977) Tetrahedrite stability relations in the Cu-Fe-Sb-S system. *American Mineralogist*, **62**, 1101–9.

Tomkins AG (2010) Wetting facilitates late-stage segregation of precious metal–enriched sulfosalt melt in magmatic sulfide systems. *Geology*, **38**, 951–4.

Tomkins AG, Pattison DRM, Frost BR (2007) On the initiation of metamorphic sulfide anatexis. *Journal of Petrology*, **48**, 511–35.

Williams-Jones AE, Migdisov AM, Sandy MA, Zhifeng X (2002) Vapor-transport of ore metals. In: *Water-rock Interactions, Ore Deposits and Environmental Geochemistry: A Tribute to David A. Crerar* (eds Hellmann R, Wood SA). Geochemical Society Special Publication, *7, 279–305*.

Wykes JL, Mavrogenes JA (2005) Hydrous sulfide melting: experimental evidence for the solubility of H_2O in sulfide melts. *Economic Geology*, **100**, 157–164.

GEOFLUIDS

Volume 12, Number 3, August 2012
ISSN 1468-8115

CONTENTS

WILEY-BLACKWELL

Geofluids* is abstracted/indexed in *Chemical Abstracts

This journal is available online at Wiley Online Library.
Visit onlinelibrary.wiley.com to search the articles and register for table of contents and e-mail alerts.